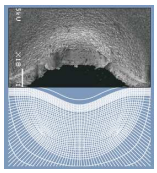

Interuniversity Master in structural integrity and durability of materials, components and structures

MASTER´S THESIS

Working title: UNDERSTANDING OF CRACK PROPAGATION MECHANISMS IN TITANIUM ALLOYS αβ

***Collaborating entity**: IRT Saint Exupéry, Toulouse – Pprime Institute, ISAE ENSMA*

***Industrial or external tutor**: Gilbert Henaff, Patrick Villechaise (ENSMA), Céline Larignon (IRT AESE)*

***Department:** Physics and Mechanics of Materials*

***Academic tutor:** Mrs.Cristina Rodríguez González*

***Department**: Department of Construction and Manufacturing Engineering*

University of Oviedo

July 2015

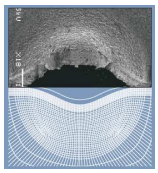

Interuniversity Master in structural integrity and durability of materials, components and structures

MASTER'S THESIS

Working title: UNDERSTANDING OF CRACK PROPAGATION MECHANISMS IN TITANIUM ALLOYS αβ

Industrial tutor name

Mr.Gilbert Henaff

Academic tutor name

Mrs.Cristina Rodríguez González

Student name

Luis Borja Peral Martínez

University of Oviedo

July 2015

PRESENTATION

➢ IRT SAINT EXUPÉRY

IRT Saint Exupéry (Technology Research Institutes) is part of the IRT Initiative launched in France in the frame of PIA (Future Invest Plan) to boost high value competitive technological sectors. 8 IRTs have been launched between 2012 and 2013.

The IRT Antoine de Saint Exupéry technology research institute brings together public and private partners in R&T activities covering three strategic domains: High Performance Multifunctional Materials, More Electrical Aircraft and Embedded Systems.

Projects develop technological blocks for the aeronautics and space industries along with embedded systems. The IRT's expertise and technology platforms and its collaborative environment help in maturing and transferring breakthrough technologies (TRL 4-6) to its industrial partners.

➢ THE ISAE ENSMA

The Ecole National Supérieure de Mécanique et d' Aérotechnique is an ISAE-group engineering school (since 2011) created in Poitiers in 1948 and installed in the Futuroscope site in 1993. The education received at the ENSMA is oriented to the aeronautical and space industry, but also to the transport industry and the energetic and mechanical industries.

Aerial view of ENSMA.

The reach of this institution goes beyond the classroom since it offers wide variety of research possibilities in collaboration with other institutions and associated laboratories such as Pprime Institute.

➢ THE PPRIME INSTITUTE

The Pprime institute, or P', is a research unit that depends on one tutelage and two partnerships, which are:

- The Nationale Research Centre (le Centre National de la Recherche Scientifique, CNRS), by means of the Engineering and Systems Sciences Institute (l'Institut des Sciences de l'Ingénierie et des Systèmes, INSIS) and the Physics Institute (l'Institut de Physique, INP).

- The University of Poitiers, that involves: The Faculty of Sciences (La Faculté des Sciences, SFA) and the National School of Engineering of Poitiers (l´Ecole Nationale Supérieure d´ Ingénieurs de Poitiers, ENSIP); and finally

- The National School of Mechanics and Aeronautics (l´Ecole Nationale Supérieure de Mécanique et de Aérotechnique, ISAE-ENSMA), already mentioned.

The Prime Institute is divided into three scientific departments:

- D1: Physics and Mechanics of Material.
- D2: Fluids, Thermal and Combustion Studies, and
- D3: Mechanics, Structures and Complex Systems.

INDEX

1 Introduction

Titanium and its alloys are widely used in industry due to their low density (4.5 gr/cm^3) and its high resistance to heat and cold. In addition, it presents a high melting point (1668°C). Titanium highlights for his low thermal capacity comparable to stainless steel, and its low coefficients of thermal expansion and conductivity. Because of its high affinity for oxygen, it is covered with a thin oxide film at ambient temperature. Thanks to this, titanium is resistant to corrosion both in saline environments and contact with acid solutions. It's a material widely used in the aeronautic industry.

Thanks to the allotropic transformation of titanium (882°C), it is possible to obtain alloys, which present a microstructure α type, β or α/β depending on the alloying elements that stabilize one or the other phase. This report has been focused on TA6V alloy, which presents a bimodal microstructure (α-β).

Understanding the interactions between microstructural parameters and damage tolerance properties of titanium alloys is one of the most relevant problems for the design of pieces in the aeronautic industry. At the moment, the titanium alloy that is the more extensively used is the TA6V (Ti-6Al-4V), for which the development of type microstructure "β" has allowed significant improvement in damage tolerance properties such as toughness or resistance to crack propagation. However, a variability is noticed in some of these properties, in spite of the control stages both the preparation and production of these pieces. Therefore the present study aims in relating the variability in crack growth resistance to microstructural parameters by a detailed examination of the interaction between cracking process and the underlying microstructure.

In the first part of this report, a brief description of the titanium alloy used is performed. Subsequently, the tests previously performed by EXOVA[1] for IRT on three specimens of type CT in accordance with ASTM E 647-11[2] standard are analyzed. Finally, the fracture surfaces of three CT specimens are analyzed using the SEM[3]. At the moment, a metallographic preparation of CT specimens has been made to observe the interaction between the microstructure and the crack path by OM[4], SEM and EBSD[5]. Thanks to this study, which is being conducted in this moment, mechanisms of crack propagation will be interpreted more easily.

[1] EXOVA is one of the world's leading providers of testing, calibration and advisory services.

[2] ASTM E 647 11: Standard Test Method for Measurement of Fatigue Crack Growth Rates.

[3] SEM: Scanning Electron Microscope.

[4] OM: Optical Microscope.

[5] EBSD: Electron Backscatter Diffraction.

2 The titanium alloy TA6V

2.1 Presentation

The titanium alloy studied is the TA6V alloy (or Ti-6Al-4V). The material composition is 6% Al and 4% V, the aluminum (Al) stabilizes the α phase and vanadium (V) stabilizes the β phase. This titanium alloy α/β is used for low temperature applications in turbo reactors, especially in low-pressure compressor aircraft reactor (figure 1).

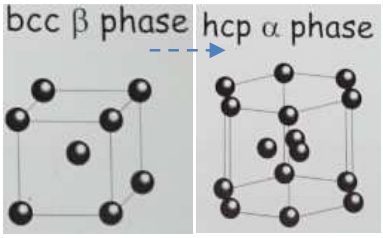

Allotropic transformation of titanium (882ºC)

Figure 1. Low-pressure compressor.

The nominal chemical composition of the alloy is presented in the following table (table 1).

	Ti	Al	V	C	Fe	O_2	N_2	Y	H_2	B	Sn+Mo+Cu+ Mn+Zr
Min.(%)	base	5.50	3.50	-	-	-	-	-	-	-	-
Max.(%)	base	6.75	4.50	0.08	0.30	0.22	0.05	0.005	0.01	0.001	0.2

Table 1. Nominal chemical composition [1].

Major conventional mechanical properties of the alloy TA6V studied are shown in the following table (table 2).

Tensile modulus E (GPa)	119
Tensile yield strength σ_y (MPa)	940
Breaking stress σ_u (MPa)	1020
Elongation at break A(%)	16.7 %

Table 2. Mechanical properties [1].

2.2 Thermomechanical treatment and microstructure

The most important parameter in thermomechanical processing and heat treatment of α-β titanium alloys is the β transus temperature. Figure 2 shows a schematic phase diagram for Ti-6Al-4V. Above the β transus the alloy is 100% β and can be relatively easily worked. However β working has, or can have, adverse effects on some mechanical properties, and so can β heat treatment. Consequently, even though initial working may be in the β phase field, final working is conventionally in the (α+β) phase field and any subsequent conventional heat treatments are also in the (α+β) phase field.

On the other hand, this is not the whole story, since the mechanical properties of α-β alloys depend on the relative amounts and distribution of the α and β phases. These variables depend strongly on the thermomechanical processing and heat treatment temperatures in the (α+β) phase field. For example, figure 2 indicates the percentage of primary α in Ti-6Al-4V at two temperatures. At the higher temperature there is less primary α and more β, which, however, contains less vanadium. Since vanadium is a β-stabilizer, this means that the higher temperature β more readily transforms to α during cooling after processing, and also during any subsequent heat treatment at relatively low temperatures, annealing at 700–750 °C.

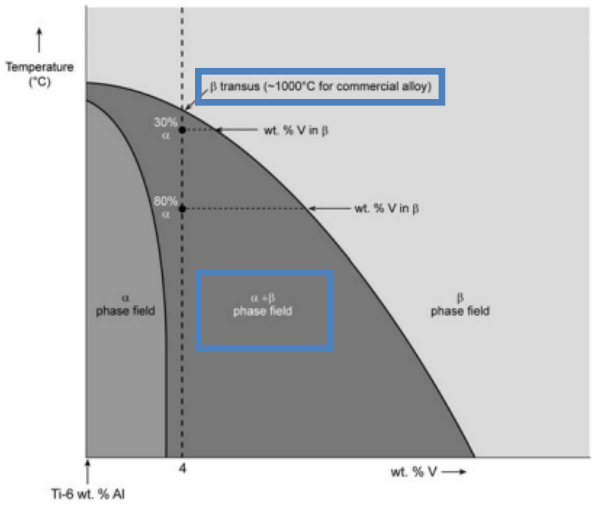

Figure 2.Schematic phase diagram for Ti-6Al-4V.

Titanium alloys α/β can present three types of different microstructure according to the thermomechanical treatment: lamellar, bimodal, equiaxial. In this section, the lamellar and bimodal microstructure are presented as a function of thermomechanical treatment.

In figure 3, the thermomechanical treatment carried out for obtaining the TA6V alloy (bimodal) is shown. When temperature alloy in the alpha-beta domain is high, a bimodal structure is obtained during cooling. Then, a structure of primary α grains in a beta matrix is obtained (see figure 4).

100ºC/min<AC<300ºC/min

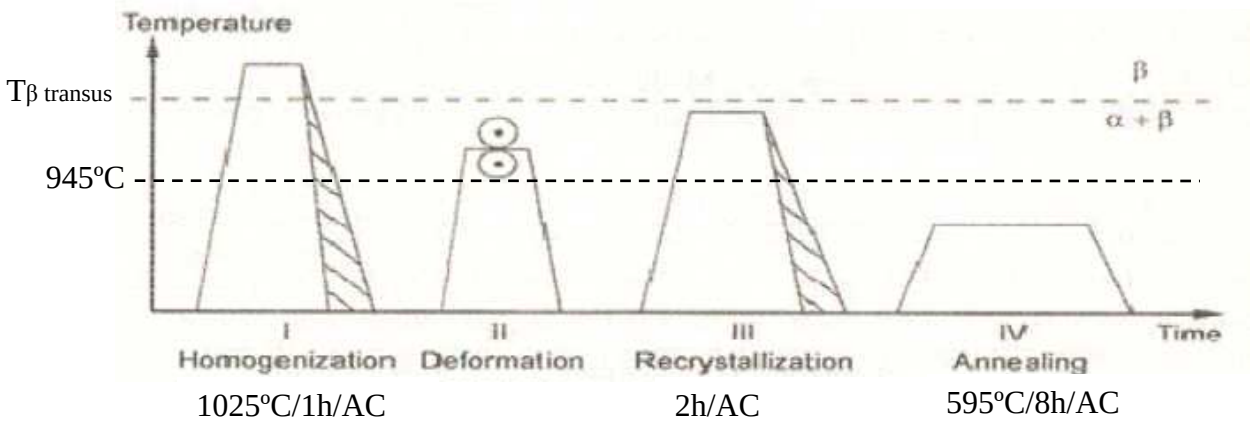

Figure 3. Thermomechanical treatment of the α+β bimodal alloy.

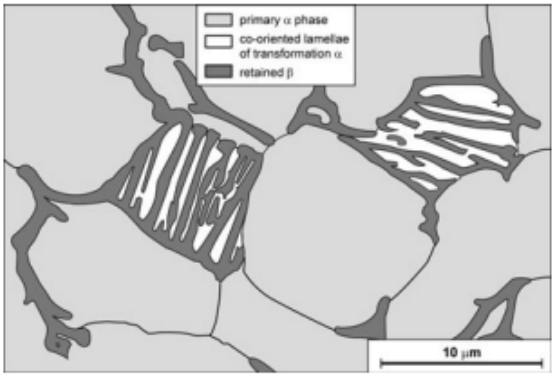

Figure 4. α/β titanium alloy bimodal microstructure.

It should be noted that the cooling rate from the domain β (step 1) determines the shape of the α platelets. These sheets are deformed in step 2 and recrystallized in step 3.

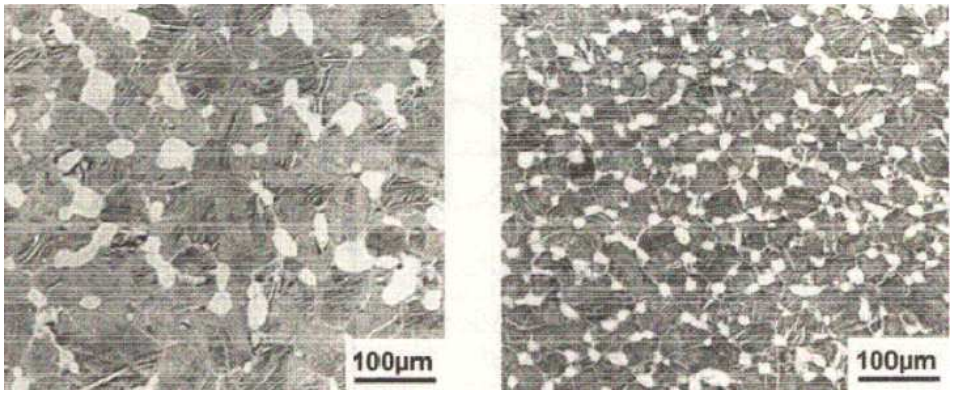

Figure 5. Influence of the cooling rate from the homogenization step.

In the left figure, an image is shown in which a slow cooling was performed whereas in the right figure, a cooling performed at higher speed is shown.

A bimodal microstructure provides greater ductility (forming) and improved resistance to fatigue crack initiation.

On the other hand, when the temperature is elevated above the transus, a lamellar microstructure can be obtained with a recrystallization in the β domain. The classic thermomechanical treatment is presented in figure 6.

100ºC/min<AC<300ºC/min

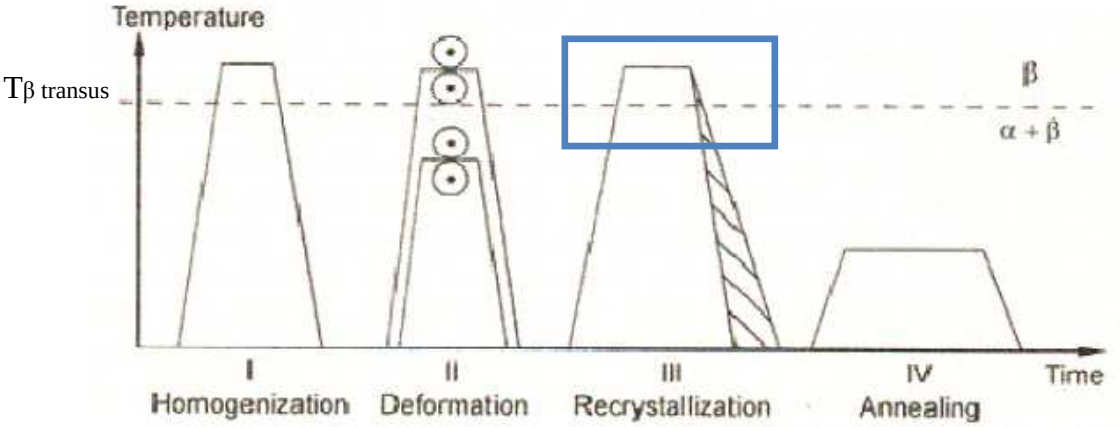

Figure 6. *Thermomechanical treatment of the α+β lamellar alloy.*

The most important parameter of this treatment is the cooling rate in the recrystallization step. If cooling is quite rapid, α platelets grow from the β grain boundary, which can generate a microstructure designed as Widmanstätten. The growth of platelets stops when another group of platelets grows in another direction. Thus, a structure of α platelets packed in a β matrix is formed. In this manner, the cooling rate affects the microstructure (see figure 7), the α size platelets, the α colony size and the thickness of these in the grain boundary.

Figure 7. α/β titanium alloy lamellar microstructure.

A lamellar microstructure provides better creep behavior, increased toughness and improved resistance to crack propagation.

3 Tests performed

To make the crack growth tests, three specimens of type CT were used. The tests were performed according to ASTM E647-11 and issue 2 specification AIMS 03-20-001[6].

3.1 Description of the CT specimens

In Figure 8, the type of CT specimen, on which the tests were performed, is shown. In table 3, the geometrical parameters and yield strength of each specimen are presented. Furthermore, it is important to note that the specimens were manufactured in two different orientations (see figure 9).

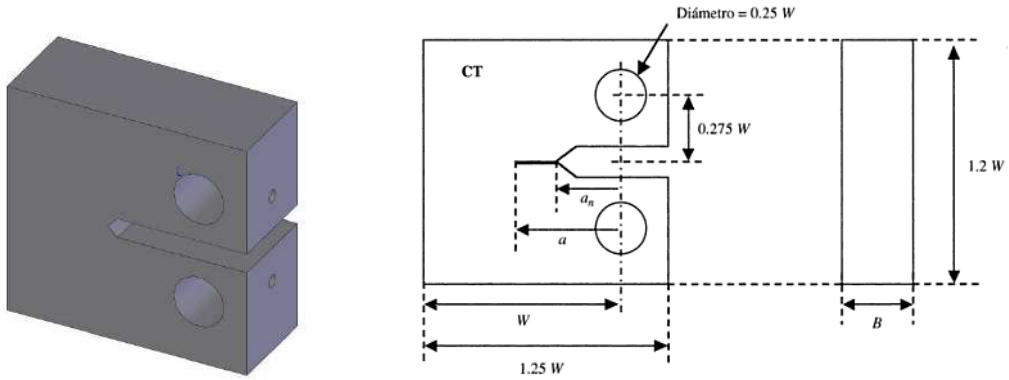

Figure 8. Specimen CT.

Specimen	Material	Orientation	Geometrical parameters			σ_y (MPa)
			a_n (mm)	B (mm)	W (mm)	
CT 302455	TA6V	L-T	18.725	12.05	75.01	870
CT 489398	TA6V	S-T	18.760	12.00	75.03	970
CT 285693	TA6V	L-T	18.830	12.05	75.04	890

Table 3.

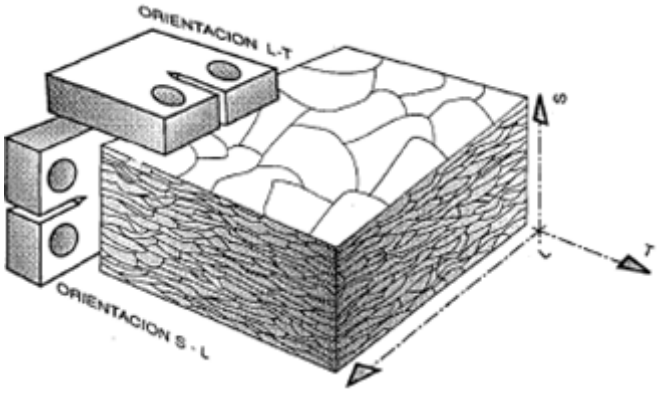

Figure 9. Orientation of CT specimens. Forging.

[6] AIMS 03-20-001: Airbus Material Specification.

3.2 Experimental tests

Prior to the fatigue test, all CT specimens were subjected to electro-erostion and a precracking procedure according to ASTM E 647.

Remember also that the ASTM E 647 standard provides a series of recommendations concerning the thickness of the CT specimens:

Recommended Thickness $\frac{W}{20} \leq B \leq \frac{W}{4}$

Suggested Min. Dimensions W= 25 mm a_n= 0.20·W

	CT 302455	CT 489398	CT 285693
W	75.01	75.03	75.04
B	12.05	12.00	12.05
W/20	3.7505	3.7515	3.752
W/4	18.7525	18.7575	18.76
0.2·W	15.002	15.006	15.008

Table 4.

As shown in Table 4, the dimensions of the CT specimens meet the recommendations of the ASTM E 647 standard in regard to the thickness.

ASTM E 647 standard establishes a procedure for obtaining fatigue behavior (Paris law) on CT specimens [4].

Basically, it divides the process in two well differentiated parts.

1. Decreasing Load Test

It is applied in propagation speed range behind 10^{-8} m/cycle. In this part, successive load steps are applied, with decreasing amplitudes of load, and therefore, of ΔK decreased and propagation velocity consequently reduced until ΔK threshold was attained ($10^{-10} \leq$ da/dN $\leq 10^{-9}$ m/cycle). Figure 10 shows a diagram of the variation of loads and ΔK during this process.

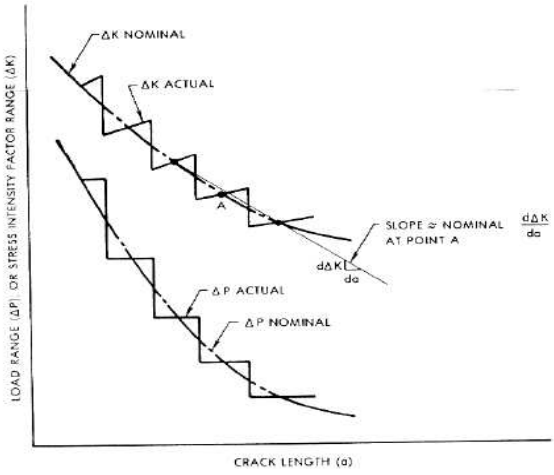

Figure 10. Decreasing Load Test.

2. Constant Load Amplitude Test

Once the threshold was attained, cycles with constant load amplitude were applied until the failure of the specimen. In this process, propagation velocity values corresponding to the high range ($da/dN \geq 10^{-9}$ m/cycle) of the Paris law are obtained. Figure 11 shows a diagram of the variation of loads and ΔK during crack propagation.

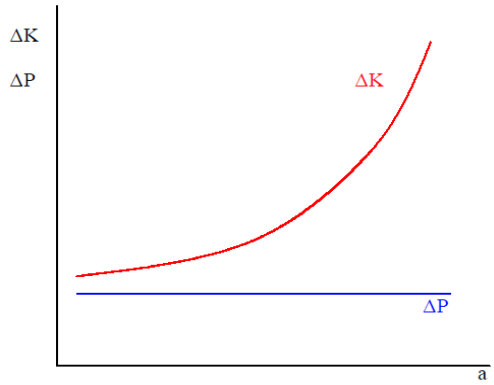

Figure 11. Constant Load Amplitude Test.

Along the test the information of the number of cycles and of the flexibility was taken regularly.

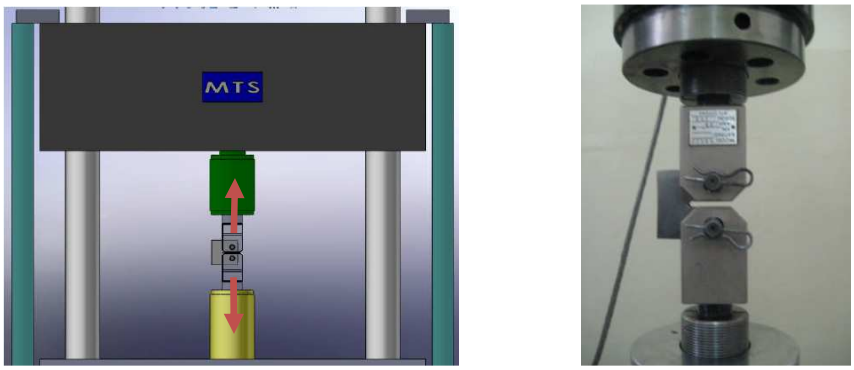

Figure 12. Implementation of the test.

In Table 5, the conditions under which the tests were performed are shown.

Specimens CT		
	Precracking	Fatigue test
Cell	±50 KN	±50 KN
Extensometer	MTS K1c Nº2	MTS K1c Nº2
Loading	Pmax.= 14 to 9 KN	Pmax.= 9 KN
R	0.1	0.1
Frequency	20 Hz	20 Hz
Temperature	22 ºC	22 ºC
Monitoring Method	COD[7]	COD

Table 5. Test conditions.

[7] COD: Crack opening displacement.

3.3 Results

The results obtained for the three CT specimens under investigation are presented in figures 13, 14 and 15. Experimental points are plotted as a function of the crack propagation rate and the tension intensity factor. On the same diagram, the points established by the AIMS 03-20-001 issue 2 specification are also presented (table 6).

	Point 1	Point 2	Point 3	Point 4
ΔK (MPa·$\sqrt{m}$)	15	20	30	40
$\frac{da}{dN}$ [$\frac{mm}{cycle}$]	4.0E-05	1.5E-04	4.0E-04	1.5E-0.3

Table 6. AIMS 03-20-001 issue 2.

This allows to check if the Paris law fitted on experimental points is placed below or above the points that are established by the AIMS specification, which will determine the conformity of a given test.

3.3.1 CT specimen 302455 L-T

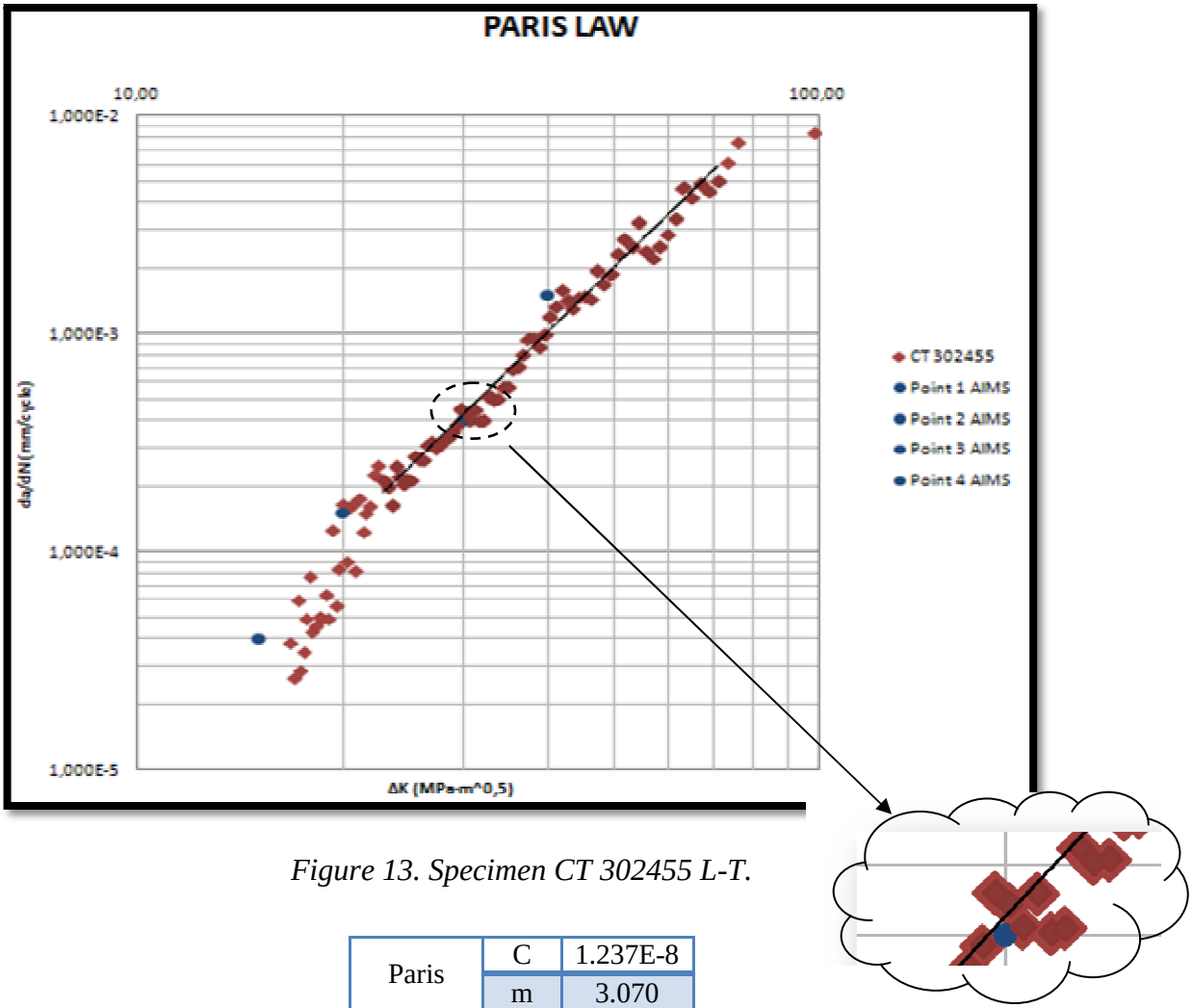

Figure 13. Specimen CT 302455 L-T.

Paris	C	1.237E-8
	m	3.070
ΔK_0 (MPa·$\sqrt{m}$)		23
ΔK_f (MPa·$\sqrt{m}$)		72

Conclusions:

The fatigue test does not satisfy the specification AIMS 03-20-001 issue 2 because there are experimental points (on the fitted Paris law) around ΔK = 30 MPa·$\sqrt{m}$ for which the crack growth rate is higher than the one established in the specification (see table 7 and figure 13).

Experimental Points		AIMS 03-20-001 issue 2	
29.67 MPa·$\sqrt{m}$	4.585E-4 mm/cycle	ΔK = 30 MPa·$\sqrt{m}$	4.0E-04 $\frac{mm}{cycle}$
30.11 MPa·$\sqrt{m}$	4.419E-4 mm/cycle		
30.58 MPa·$\sqrt{m}$	4.108E-4 mm/cycle		

Table 7.Comparison between experimental points and specification.

3.3.2 CT specimen 489398 S-T

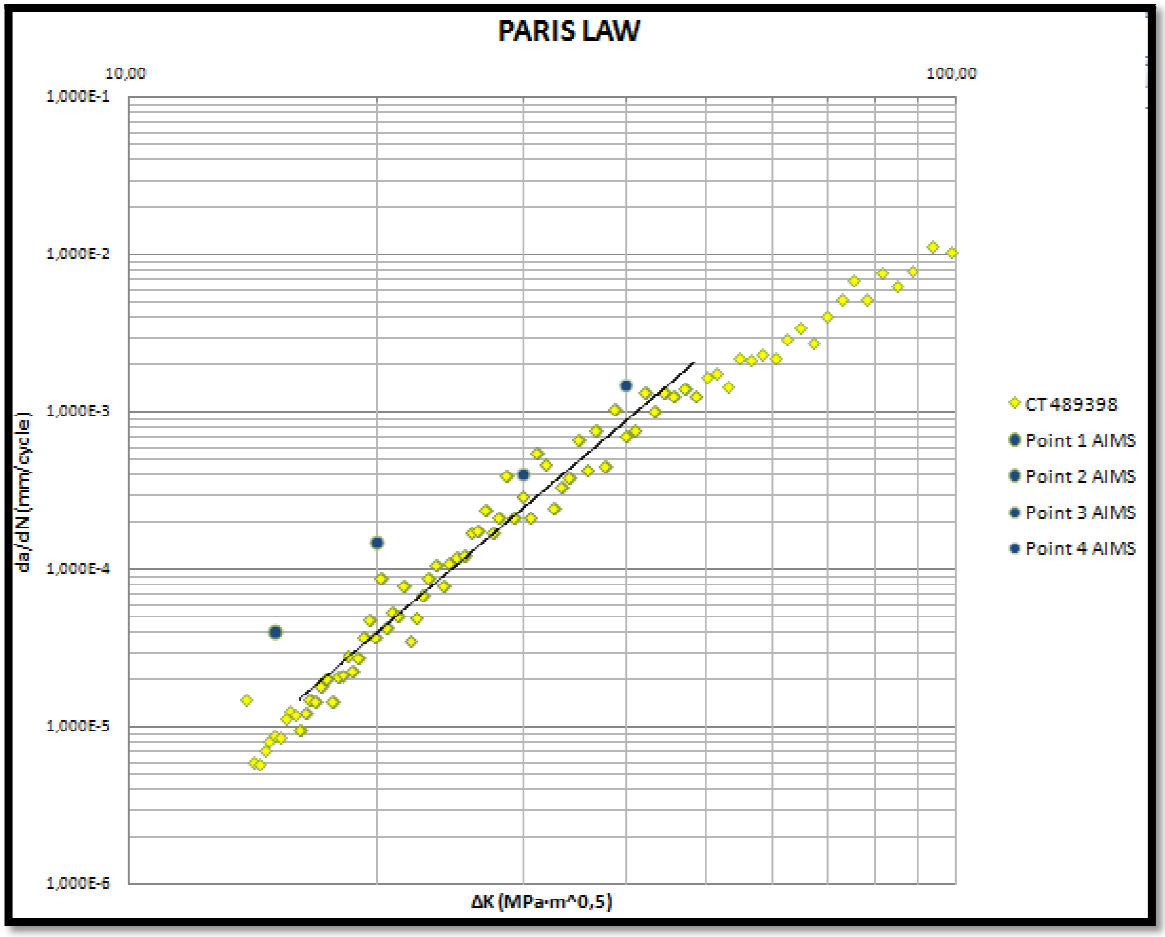

Figure 14. Specimen CT 489398 S-T

Paris	C	4.940E-11
	m	4.537
ΔK_0 (MPa·$\sqrt{m}$)		16
ΔK_f (MPa·$\sqrt{m}$)		48

Conclusions:

The fatigue test satisfies the specification AIMS 03-20-001 issue 2 because the Paris law crack growth rates derived from experimental points are lower than the ones established by AIMS once the Paris law adjustment was performed.

3.3.3 CT specimen 285693 L-T

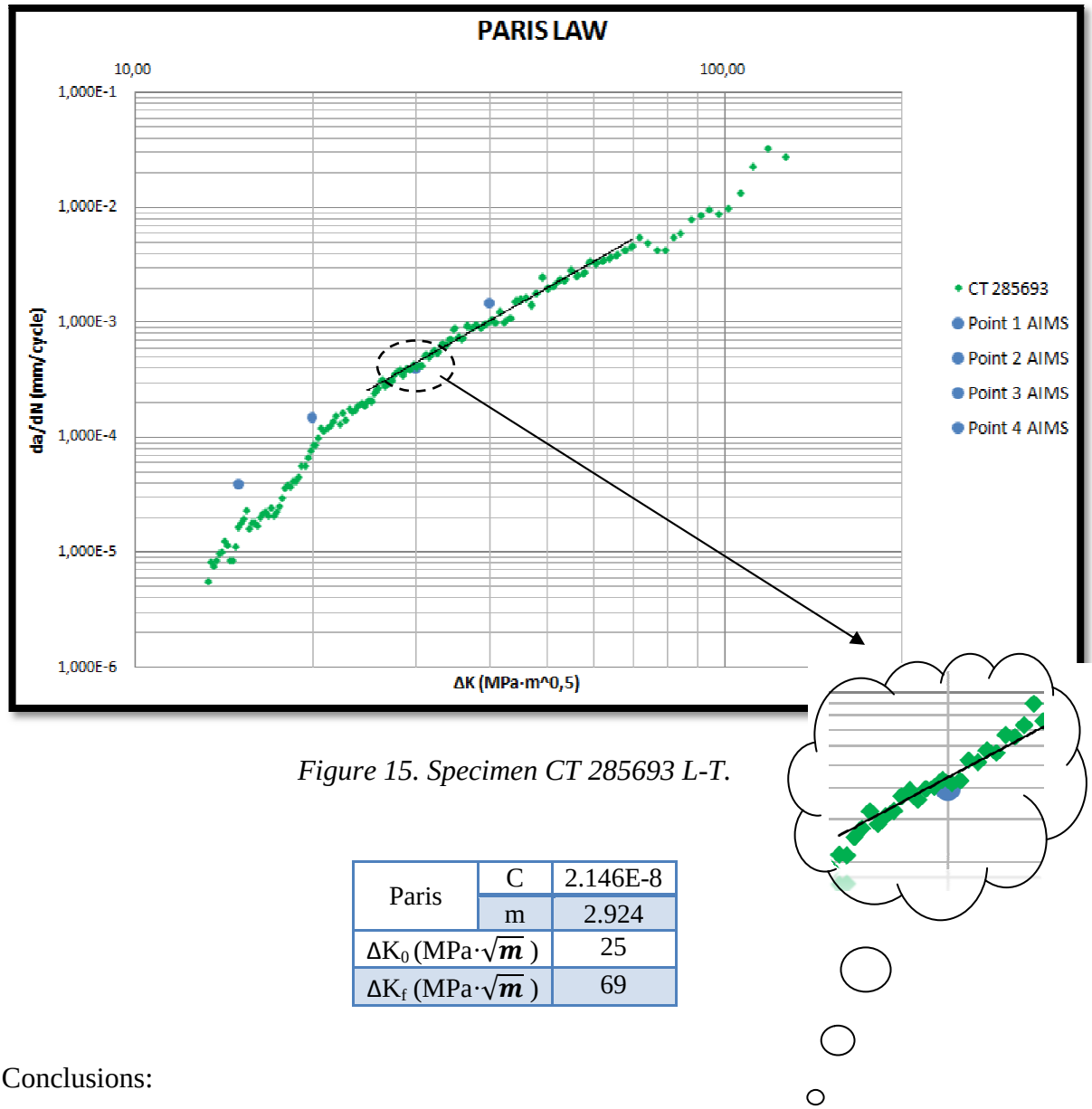

Figure 15. Specimen CT 285693 L-T.

Paris	C	2.146E-8
	m	2.924
ΔK_0 (MPa·$\sqrt{m}$)		25
ΔK_f (MPa·$\sqrt{m}$)		69

Conclusions:

The fatigue test does not satisfy the specification AIMS 03-20-001 issue 2 because there are experimental points between ΔK = 25 MPa·$\sqrt{m}$ and ΔK = 35 MPa·$\sqrt{m}$ for which the crack growth rate is higher than established in the specification AIMS 03-20-001 issue 2 (see figure 15). In table 8, some experimental points, which don't satisfy the specification, are shown.

Experimental Points		AIMS 03-20-001 issue 2	
29.73 MPa·$\sqrt{m}$	4.362E-4 mm/cycle	ΔK = 30 MPa·$\sqrt{m}$	4.0E-04 $\frac{mm}{cycle}$
30.18 MPa·$\sqrt{m}$	4.197E-4 mm/cycle		
34.79 MPa·$\sqrt{m}$	8.982E-4 mm/cycle		

Table 8.Comparison between experimental points and specification.

The main aim of the present study is to determine the microstructural sources of such discrepancies from one specimen to another. In a first step, a detailed characterization of the fracture surfaces has been carried out and is presented in the next section (section 4).

4 Observation of the fracture surface for different values of ΔK

Different observations on the fracture surface of the CT specimens were made by scanning electron microscope JSM-6400 (see figure 17). The observations were performed at different values of ΔK, which are specified by AIMS 03-20-001 (Airbus Material Specification). In the following sections (4.1, 4.2 and 4.3) an analysis of the various phenomena observed during crack propagation is shown.

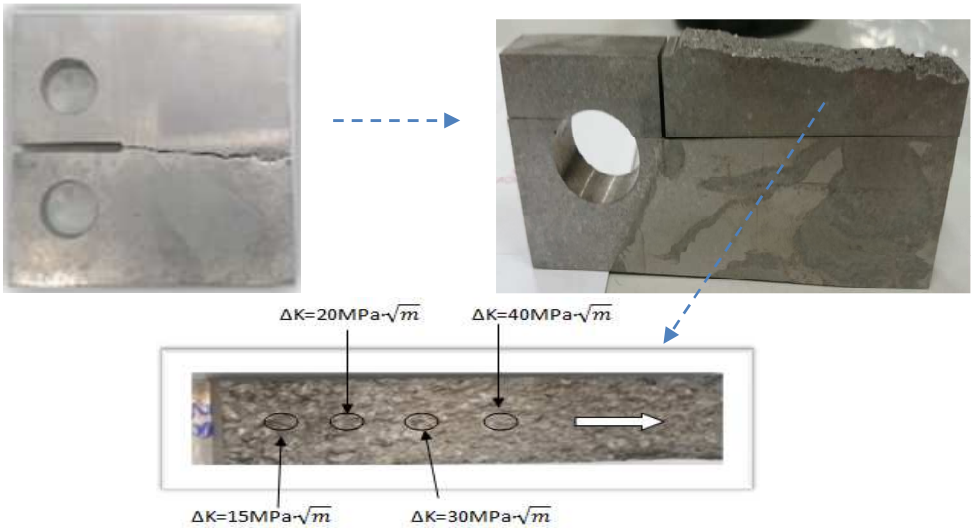

Figure 16.Fracture surface.

On the basis of the relation between the crack length (a_m) determined in the fatigue test and the corresponding value of ΔK (MPa$\sqrt{m}$), Δa (mm) can be determined taking into account the notch length is know ($\Delta a = a_m - a_n$). In this manner, we can locate the SEM points of interest (see table 9).

CT specimen	AIMS 03-20-001 issue 2 ΔK (MPa·$\sqrt{m}$)	a_n (mm)	a_m (mm)	Δa (mm)
302455 L-T	15	18.725	24.90	6.175
	20	18.725	33.01	14.285
	30	18.725	42.88	24.155
	40	18.725	48.22	29.495
489398 S-T	15	18.760	24.78	6.02
	20	18.760	32.83	14.07
	30	18.760	42.69	23.93
	40	18.760	48.07	29.31
285693 L-T	15	18.830	25.10	6.27
	20	18.830	33.11	14.28
	30	18.830	42.95	24.12
	40	18.830	48.26	29.43

Table 9.Crack increments corresponding to the points of interest.

Figure 17. Scanning electron microscopy JSM-6400.

To observe the fracture surface of the titanium alloy TAV6 in the SEM, different operations were carried out. CT specimens were cut with the ISOMET 4000, and later introduced in a container with acetone, which was introduced in the ULTRASONIC 120 T for 10 minutes to remove particles that have been deposited on the surface of interest during the cutting operation. The cut was made with a diamond disc (11-4217-010) suitable for cutting titanium alloy TA6V. During the cutting operation, water has been used as a lubricant.

Figure 18. ISOMET 4000.

Figure 19. ULTRASONIC 120 T.

4.1 CT specimen 302455 L-T

In figures 20, 21, 22 and 23 various observations of the fracture surface as a function of ΔK are shown.

Direction of propagation

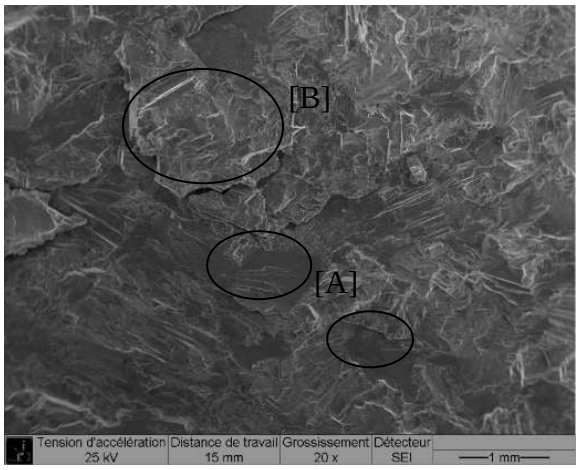

Figure 20. $\Delta K=15\ MPa\cdot\sqrt{m}\ .\ \frac{da}{dN}=2.458\cdot 10^{-5}\ \frac{mm}{cycle}$

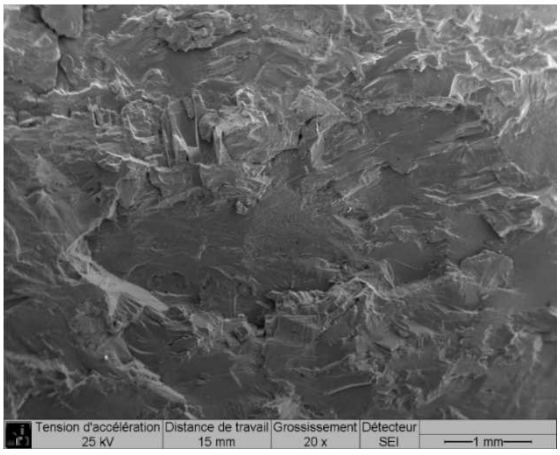

Figure 21. $\Delta K=20\ MPa\cdot\sqrt{m}\ .\ \frac{da}{dN}=1.688\cdot 10^{-4}\ \frac{mm}{cycle}$

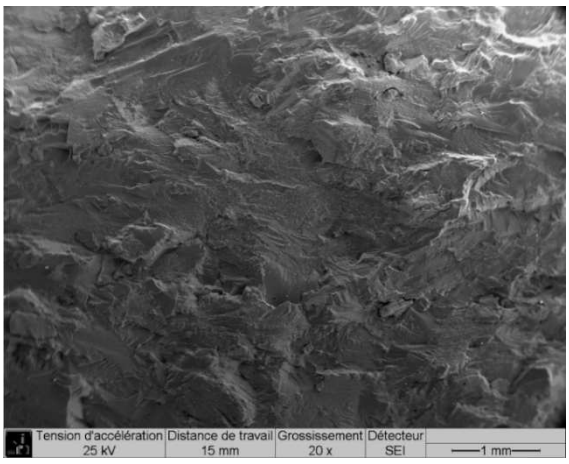

Figure 22. $\Delta K=30\ MPa\cdot\sqrt{m}\ .\ \frac{da}{dN}=4.419\cdot 10^{-4}\ \frac{mm}{cycle}$

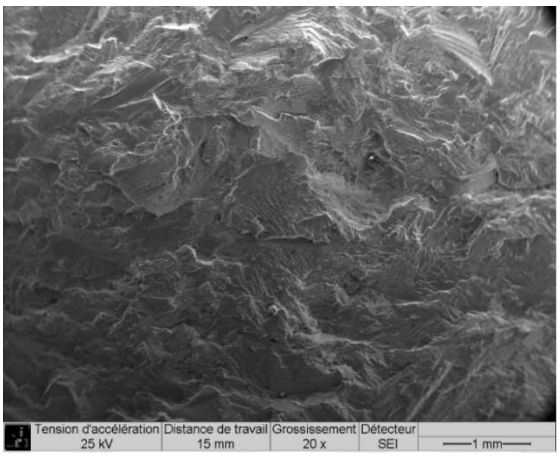

Figure 23. $\Delta K=40\ MPa\cdot\sqrt{m}\ .\ \frac{da}{dN}=1.225\cdot 10^{-3}\ \frac{mm}{cycle}$

On the same fractographies, some of the propagation mechanisms observed are detailed.

Numerous cleavage facets which are characteristic of a brittle-type propagation [A] can be observed on the fracture surface. Direct separation of cristallographic planes produces smooth, shiny and different angle-orientation facets, thus, macroscopically the fracture surface has a granular and bright aspect (see figure 24).

Figure 24. Granular and shiny fracture surface.

On the same surfaces, areas with larger plastic deformation [B] are observed. There, a propagation mechanism of mixed type (pseudo-cleavage) is defined.

At the microscopic level, the passage of the crack across the grain produces a fine topography of the facet where river marks can be seen (see figure 25). The origin of the river marks is due to the interconnection of cleavage planes located at different levels, as the crack advances, a small step is produced in the intersection to maintain the continuity during crack propagation.

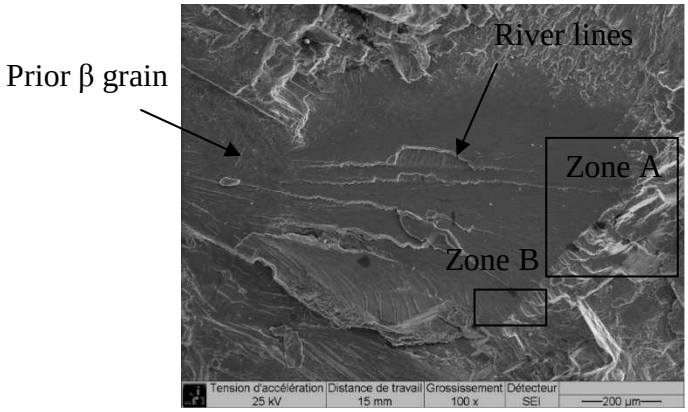

Figure 25. Detail of the fracture surface for $\Delta K=15MPa\cdot\sqrt{m}$. River marks running parallel to the crack growth direction.

In Figure 26, the transition between two adjacent β grains with different orientation is observed, while in figure 27, typical furrows caused by the propagation of the crack are recognized [6]. These furrows are formed as a result of trans-lamellar or inter-lamellar propagation on the α platelets. Following these observations, longitudinal section in the middle of the CT specimen (see section 5-work in progress) is performed in order to observe the interaction between the microstructure and the crack path. In this way, we will be able to decide if it is a trans-lamellar or inter-lamellar propagation.

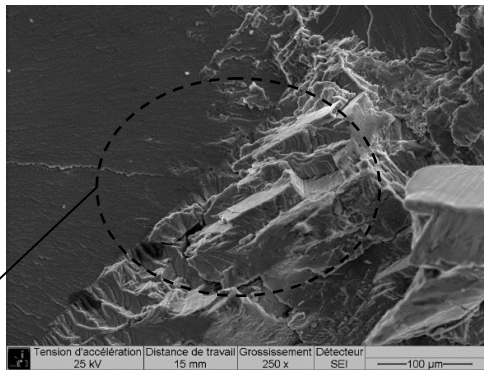

Figure 26. Zone A. Transition between two adjacent β grains.

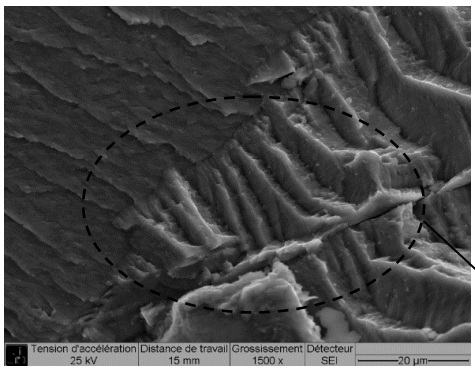

Figure 27. Zone B. Furrows.

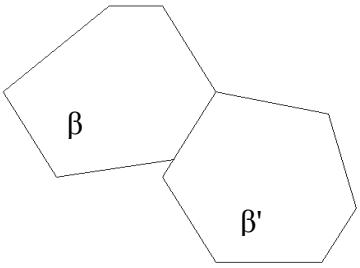

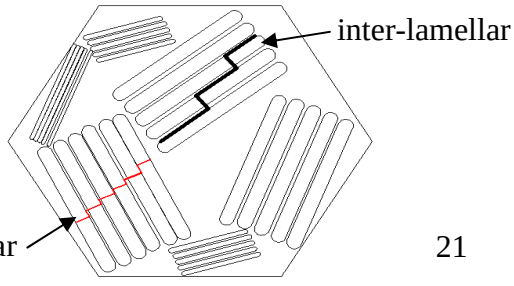

A variation of the striation morphology which occurred for ΔK=20 MPa·$\sqrt{m}$, consisted of rather indistinct line criss-crossing the fracture surface. This morphology was designated as ‘’cross-hatch’’ (see figure 28) [6].

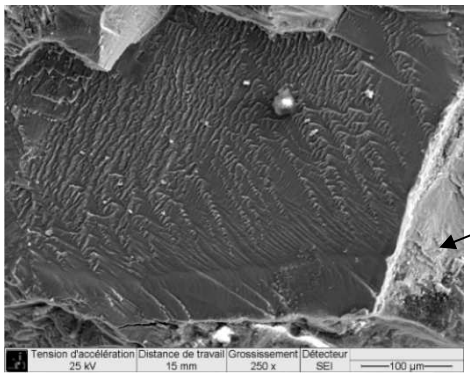

Figure 28. Cross-hatch.

In figures 29 and 30, two details of the fracture surface for ΔK=30 MPa·$\sqrt{m}$ are shown. In figure 29, a transition zone due to the different orientation of the α colonies is noted, whereas in figure 30, typical striations [6] produced in a fatigue process are recognized, these were observed in flat areas, from values $\frac{da}{dN} \geq 4.419 \cdot 10^{-4}\ \frac{mm}{cycle}$.

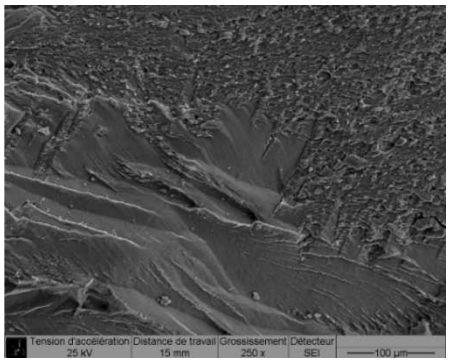

Figure 29.

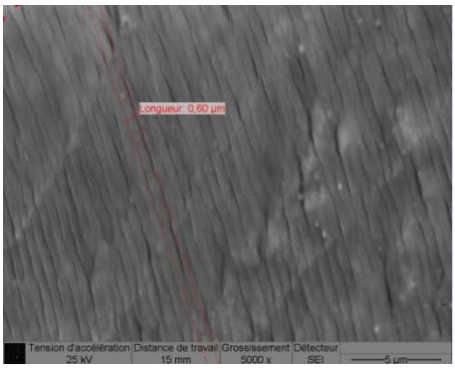

Figure 30. Striations.

As the propagation velocity increases, striations become more visible (see figure 31).

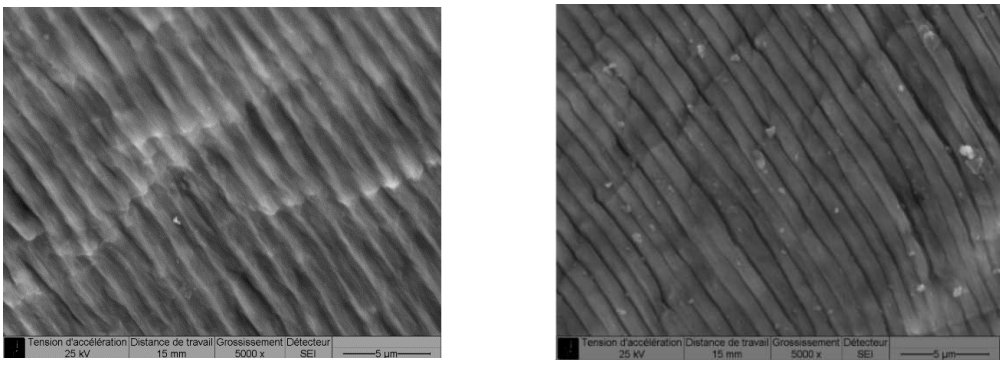

Figure 31. Striations for ΔK=40 MPa·$\sqrt{m}$ ($\frac{da}{dN}$ = 1.225· $10^{-3}\ \frac{mm}{cycle}$)

4.2 CT specimen 489398 S-T

In figures 32, 33, 34 and 35 various observations of the fracture surface as a function of ΔK are shown.

Direction of propagation

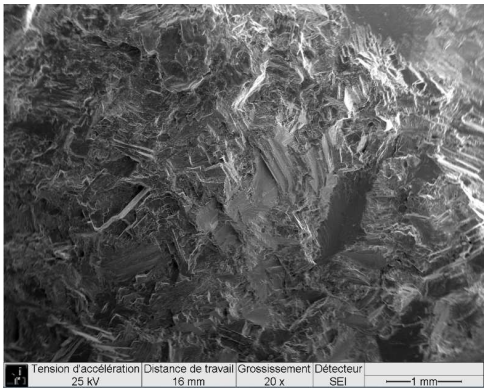

Figure 32. ΔK=15 MPa$\sqrt{m}$. $\frac{da}{dN}$ = 8.950∗ 10^{-6} $\frac{mm}{cycle}$

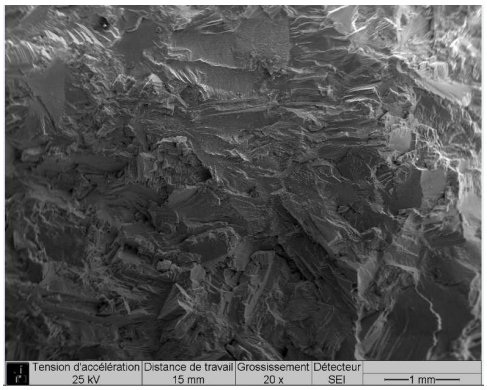

Figure 33. ΔK=20 MPa$\sqrt{m}$. $\frac{da}{dN}$ = 3.750∗ 10^{-5} $\frac{mm}{cycle}$

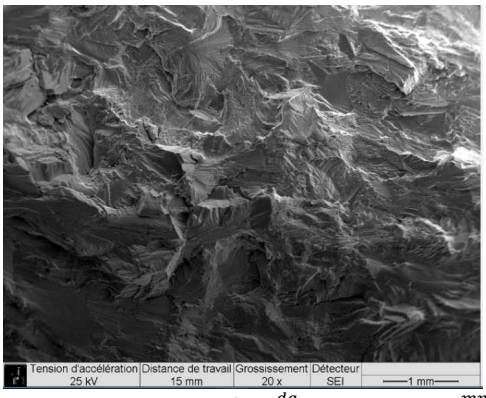

Figure 34. ΔK=30 MPa$\sqrt{m}$. $\frac{da}{dN}$ = 2.895∗ 10^{-4} $\frac{mm}{cycle}$

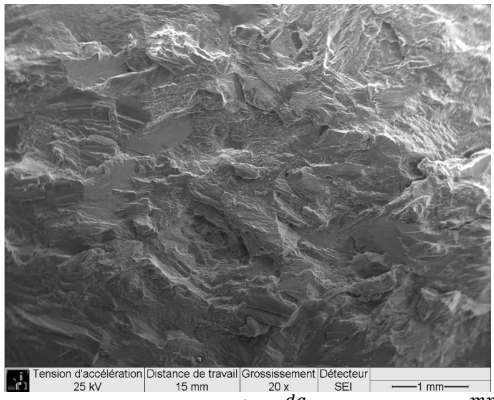

Figure 35. ΔK=40 MPa$\sqrt{m}$. $\frac{da}{dN}$ = 7.024∗ 10^{-4} $\frac{mm}{cycle}$

As well as in the CT 302455 specimen, pseudo-cleavages can be observed on the fracture surface as a result from a damage mechanism of mixed type due to the presence of brittle areas alternating with areas having greater plastic deformation presumably due to variation in crystallographic orientation with respect to the main crack plane.

In Figures 36 and 37, details of the fracture surface for ΔK = 15 MPa·$\sqrt{m}$ are shown. In figure 36, various facets generated as a result of cleavage are observed, two different modes of propagation, trans-lamellar and inter-lamellar are observed on the steps of cleavage which were generated by the rotation of the cleavage plane as it has to rotate to maintain continuity in the propagation.

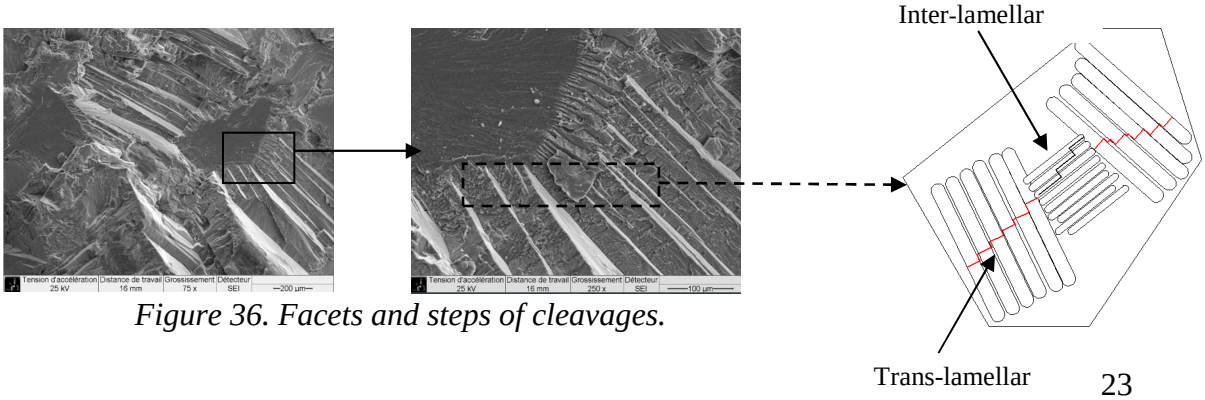

Figure 36. Facets and steps of cleavages.

In figure 37, another facet of cleavage in which a change in the transition zone can be observed due to the appearance of a trans-lamellar or inter-lamellar propagation. As mentioned above, a longitudinal section (see section 5-work in progress) in the middle of the CT specimen will be performed to determine in a later study if the propagation is trans-lamellar or inter-lamellar.

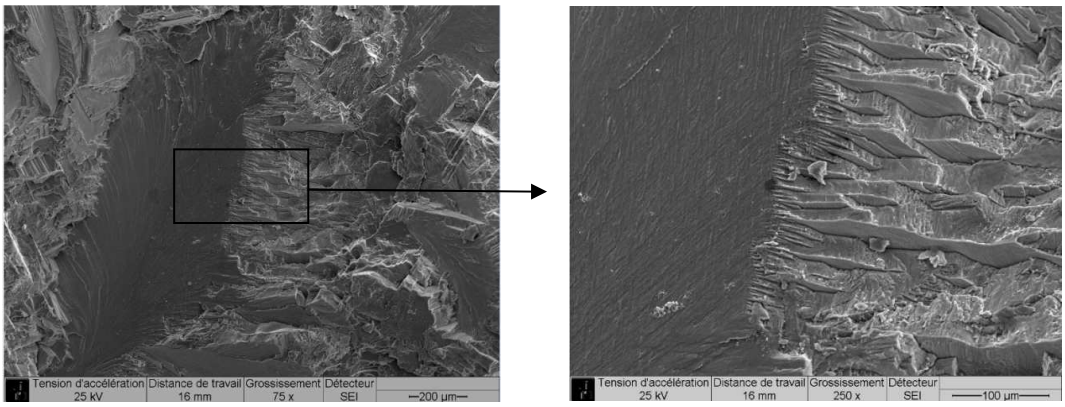

Figure 37.Facet cleavage.

Different aspects of the fracture surface for ΔK = 20 MPa$\sqrt{m}$ are shown in figure 38.

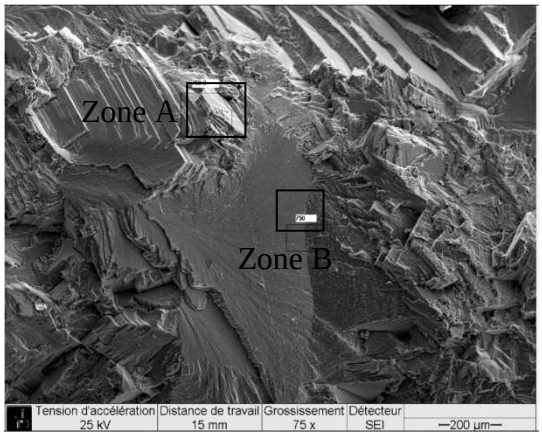

Figure 38.See locations of zones A and B.

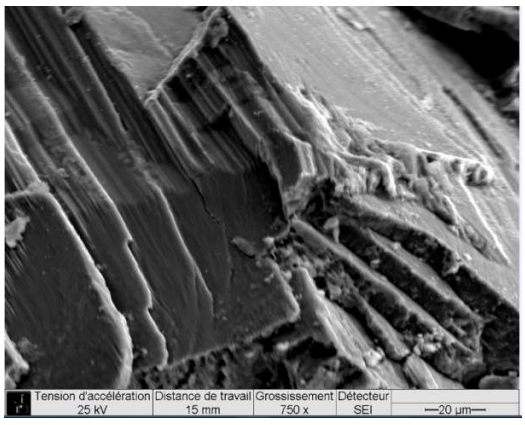

Zone A. Steps of cleavage.

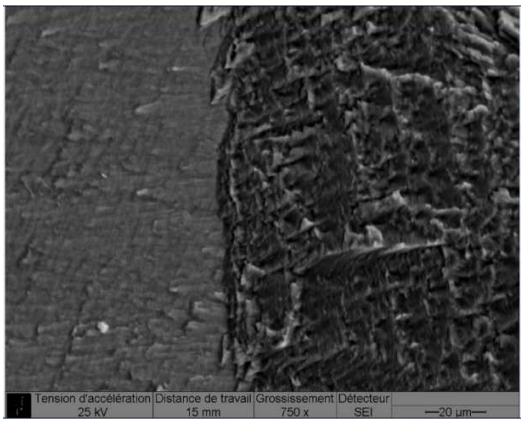

Zone B. Cross-hatch.

As it was discussed previously, the steps of cleavage (see zone A, figure 38) are generated by the rotation of the cleavage plane as it has to rotate to maintain continuity in the propagation.

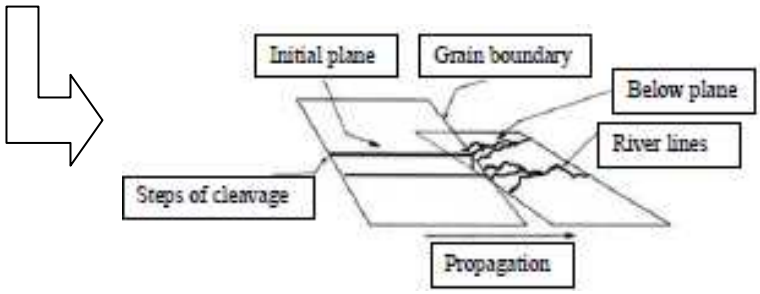

For ΔK = 30 MPa$\sqrt{m}$, a detail of the fracture surface is presented in which different modes of propagation can be seen (see figure 39). On the flat areas, fine striations become visible for $\frac{da}{dN}$ = 2.895∗ 10^{-4} $\frac{mm}{cycle}$ (see figure 40).

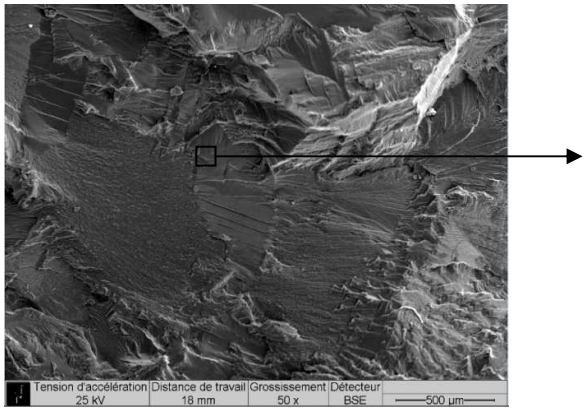

Figure 39.

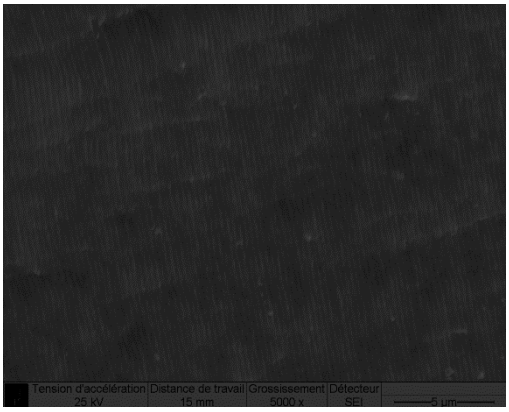

Figure 40. Striations.

For ΔK = 40 MPa· $\sqrt{m}$, as the propagation rate increases, striations become more noticeable for $\frac{da}{dN}$ = 7.024∗ 10^{-4} $\frac{mm}{cycle}$ (see figure 41).

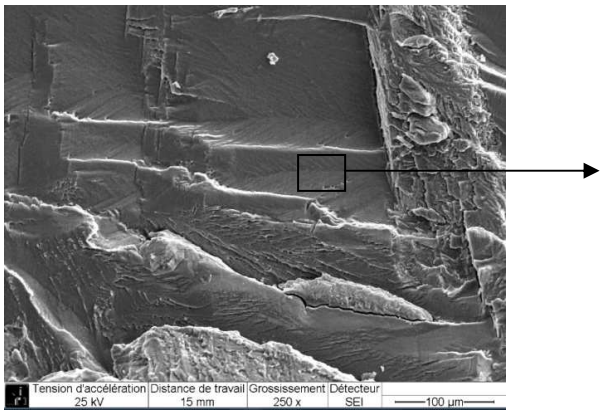

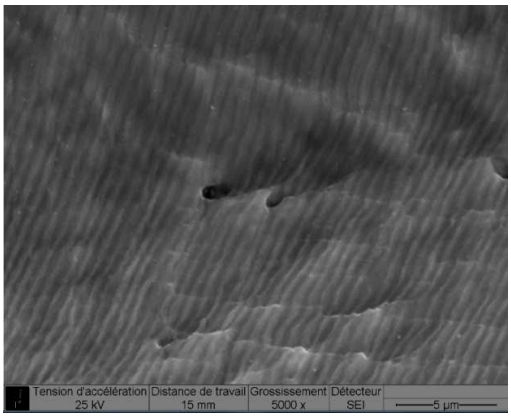

Figure 41. Striations.

4.3 CT specimen 285693 L-T

In figures 42, 43, 44 and 45 various observations of the fracture surface as a function of ΔK are shown.

Direction of propagation

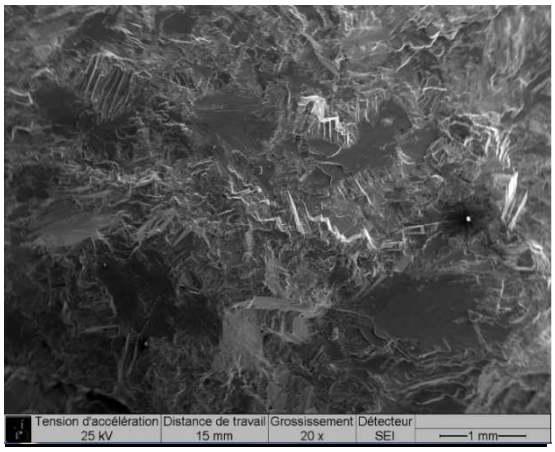

Figure 42. ΔK=15 MPa$\sqrt{m}$. $\frac{da}{dN}$ =1.801∗ 10^{-5} $\frac{mm}{cycle}$

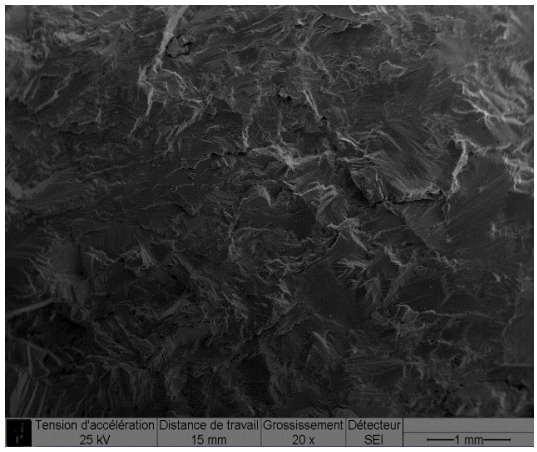

Figure 43. ΔK=20 MPa$\sqrt{m}$. $\frac{da}{dN}$ =8.756∗ 10^{-5} $\frac{mm}{cycle}$

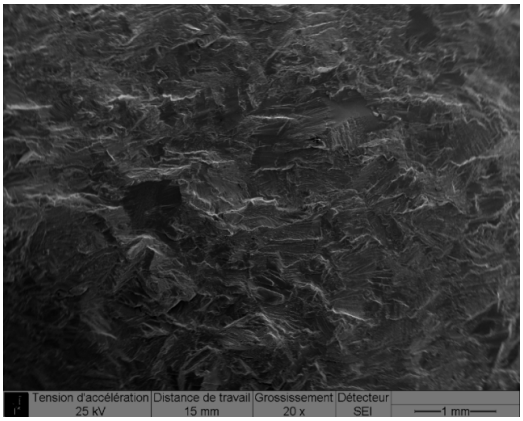

Figure 44. ΔK=30 MPa$\sqrt{m}$. $\frac{da}{dN}$ =4.197∗ 10^{-4} $\frac{mm}{cycle}$

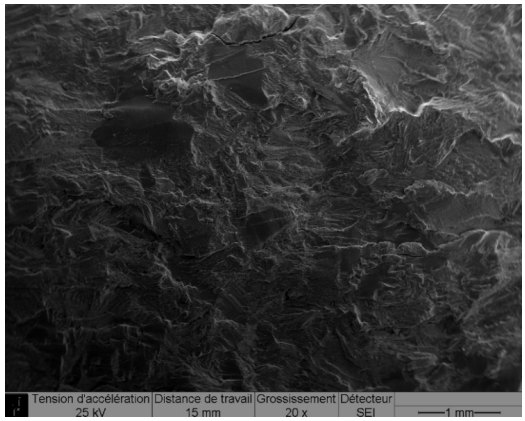

Figure 45. ΔK=40 MPa$\sqrt{m}$. $\frac{da}{dN}$ =1.072∗ 10^{-3} $\frac{mm}{cycle}$

Pseudo-cleavages can be observed as a result of a damage mechanism mixed type. Some details of the fracture surface for different values of ΔK are shown below.

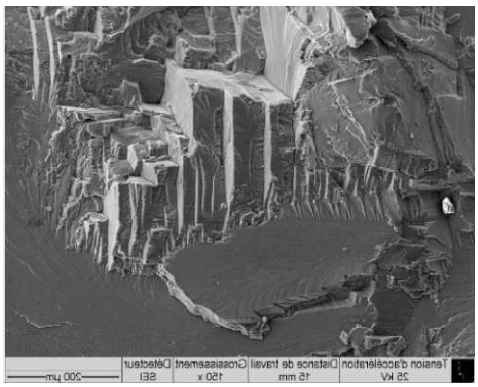

Figure 46.ΔK=15 MPa$\sqrt{m}$. Facets and steps of cleavage.

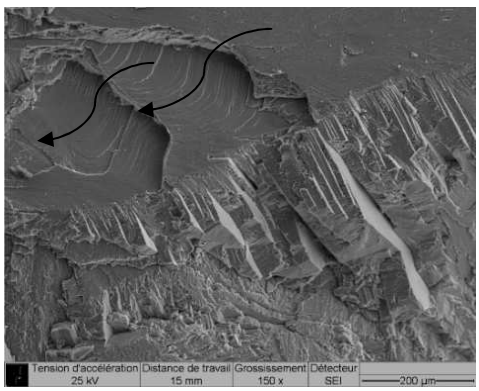

Figure 47. ΔK=15 MPa$\sqrt{m}$ Different modes of propagation.

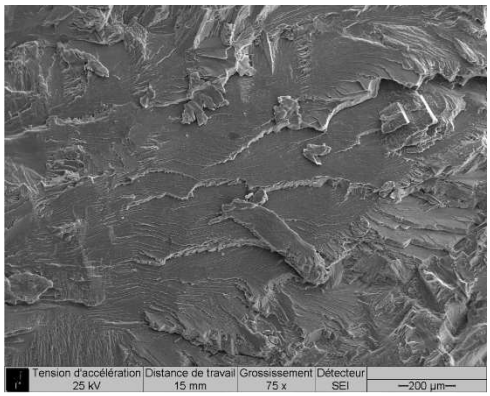

Figure 48. ΔK=20 MPa$\sqrt{\text{m}}$.

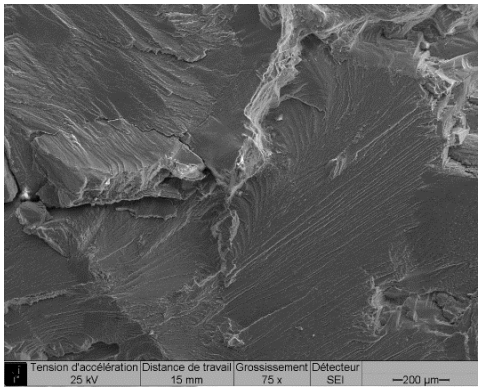

Figure 49. ΔK=20 MPa$\sqrt{\text{m}}$.

For ΔK=30 MPa· $\sqrt{m}$, some details of the fracture surface are shown below (figures 50 and 51). On the flat areas, striations have appeared for $\frac{da}{dN}$ =4.197· 10^{-4} $\frac{mm}{cycle}$ (see figure 52).

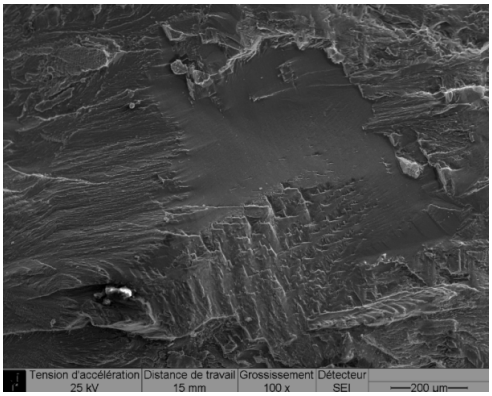

Figure 50. Different modes of propagation.

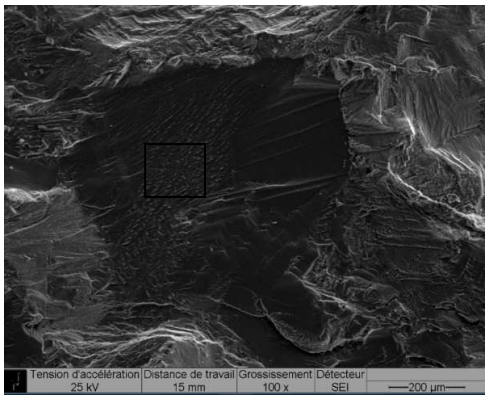

Figure 51. Cross-hatch.

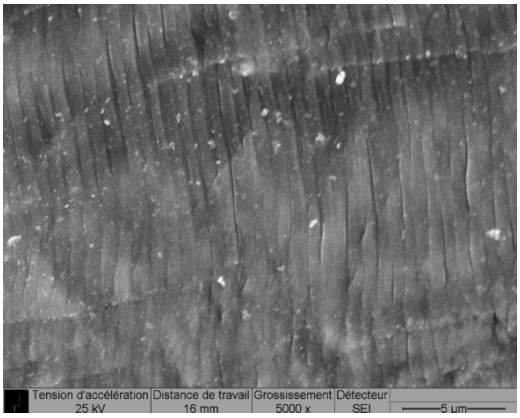

Figure 52. Striations.

As it was also obseved in the other CT specimens, as the growth rate increases, striations become more visible. Striations are formed as a result of the stress distribution in the crack front. In the case of crystalline materials, there is a restriction on the possible slip planes, and then striations are formed when the sliding system is

conveniently oriented with respect to the acting stress. If the crystal grain is oriented unfavorably, striations are missing or poorly defined.

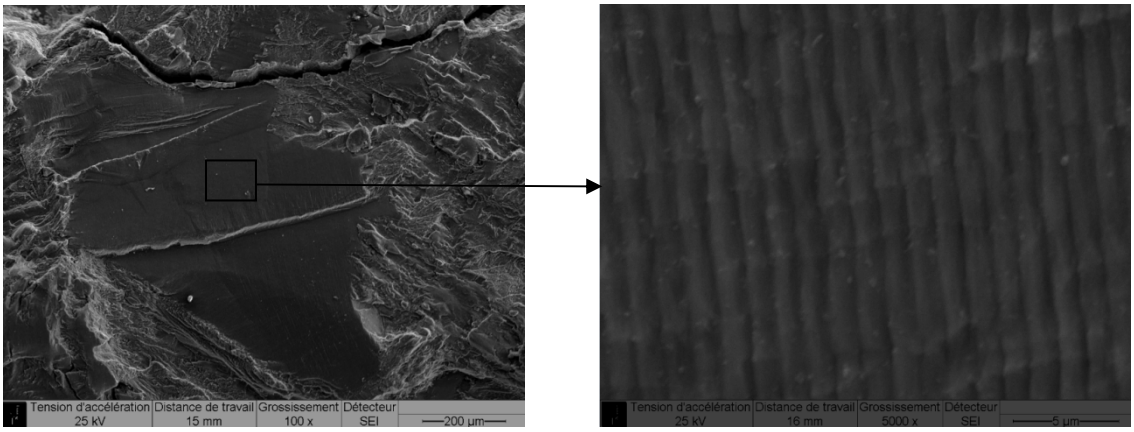

Figure 53. ΔK=40 MPa$\sqrt{m}$. $\frac{da}{dN}$ *=1.072∗* 10^{-3} $\frac{mm}{cycle}$. *Striations located on the facet.*

4.4 Conclusions

The main mechanism of brittle fracture is the cleavage which is the direct separation of crystalline planes by atomic bond breaking. The fracture plane is called cleavage plane. The most representative model of the cleavage consists in a pair of parallel rows of atoms, which are separated by a normal stress, as shown in figure 54. It is understood then that the cleavage is caused mainly by normal stresses and gives way to fracture mode I. On the fracture surfaces of the CT specimens were observed brittle areas and areas with larger plastic deformation (presumably due to variation in crystallograplic orientation with respect to the main crack plane) were observed, as one of the characteristics of titanium alloys is that before cleavage occurs, plastic deformation is produced.

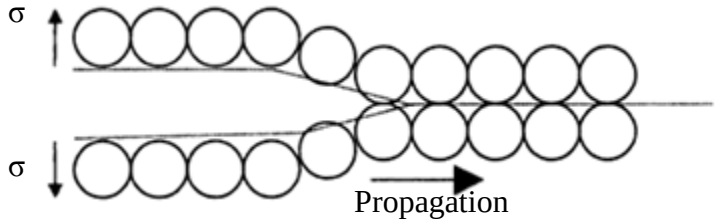

Figure 54. Cleavage

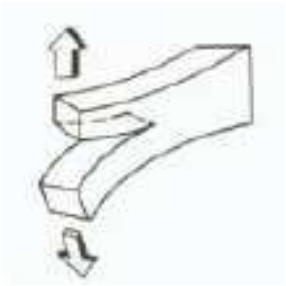

Figure 55. Mode I fracture.

In all the examined specimens, the crack growth was trans-granular in nature**.** On the fracture face it was possible to distinguish several distinct types of fracture morphologies. Indeed propagation mechanisms as cleavage-like facet [6], striations, furrows and cross-hatch were observed on the fracture surface.

Regarding the fatigue tests performed, the only CT specimen that checked the fatigue specifications according to AIMS was the 489398 CT specimen machined with the S-T orientation. This specimen presented more irregular propagation mode (see figures 36 and 38). Because of this, when the crack meets an obstacle, it has to find another sliding plane to continue the propagation. This may delay the propagation, leading to higher crack growth resistance. On the other hand, CT specimens with the L-T orientation present several flat areas which facilitate the crack propagation. In this manner, as it can be seen in figure 56, it can be observed that the crack growth rate in the S-T orientation specimen is lower than the crack growth rate determined in the CT specimens with L-T orientation.

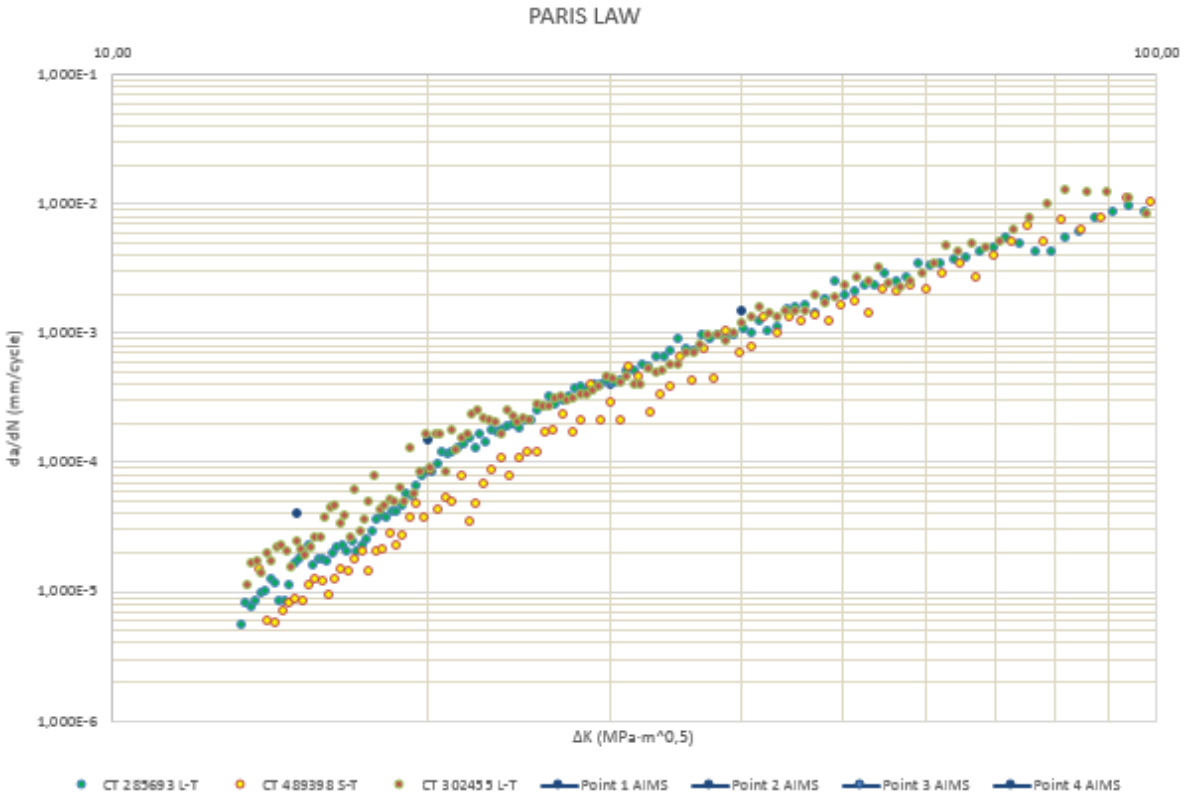

Figure 56. Paris law obtained with specimens with different orientation.

5 Work in progress

As a first step, the fracture surfaces of CT specimens were observed by SEM. Interpreting the propagation mechanisms observing only the fracture face is a difficult task, so that a longitudinal section in the middle of the CT specimens was performed to observe the interaction between the microstructure and the crack path (see figure 57). In a second step, this will be helpful to interpret better many of the points that have been commented in the chapter 4.

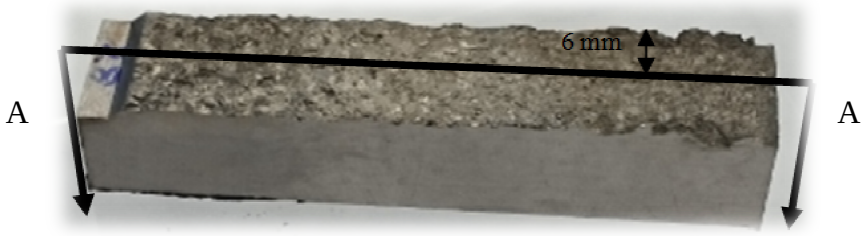

Figure 57. Fracture surface. Longitudinal section A-A.

Once the longitudinal section was performed with the ISOMET 4000, the interior face of CT specimens was polished with different abrasive papers (320-500-1000-2400-4000) on the polisher. Afterwards, chemical attack with hydrofluoric acid was performed (0.5 cm^3 of hydrofluoric acid 40%, 99.5 cm^3 distilled water, cotton wool 15 seconds)

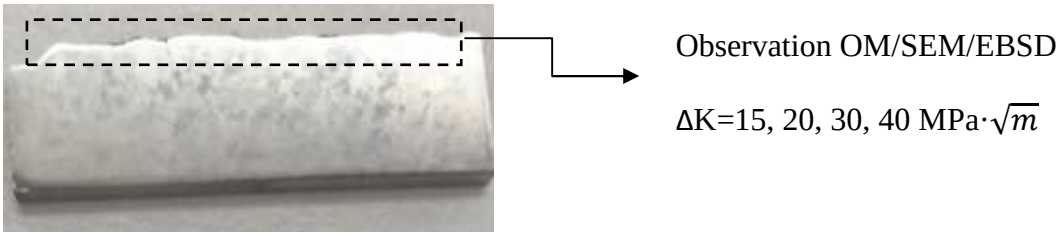

Figure 58. Interior face of CT specimen.

Finally, using optical microscope (OM) and the scanning electron microscopy (SEM), several correlative observations of the microstructure for ΔK = 15, 20, 30 and 40 MPa·$\sqrt{m}$ will be made. These observations will be related to the facts established in the chapter 4 (observation of the fracture surface). As a result, some of the hypotheses formulated in the chapter 4 will be supported or disregarded.

Figure 59. Polisher.

Later on, the study will be completed with a cross-section analysis, which will help to interpret the relationship between microstructure and crack path, will be realized. In addition, the EBSD technique will be applied on the CT specimens to determine the crystallographic texture.

6 Bibliography

[1], [2] J.Méndez et P.Villechaise, Analyse expérimentale des modes de deformation et d'endommagement par fatigue à 20°C d'alliages de titane. Aspects cristallographiques à différentes échelles, Université de Poitiers, 2006.

[3] R. Wanhill and S. Barter, Fatigue of Beta Processed and Beta Heat-treated, Titanium alloys, Springer Briefs in Applied Sciences and Technology 2012.

[4] ASTM E 647, "Standard Test Method for Measurement of Fatigue Crack Growth Rates". ASTM, Annual Book of ASTM Standards, Vol.03.01, pag.557- 593, (1997).

[5] S.Cicero, J.A.Álvarez y F.Gutiérrez-Solana, determinación de la velocidad de propagación de fisuras en aleaciones de aluminio. Problemática encontrada en la aplicación de la norma ASTM E-647, Anales de Mecánica de la fractura, Vol.20 (2003).

[6] C.M Ward-Close and C.J. Beevers, the influence of grain orientation on the mode and rate of fatigue crack growth in α-Titanium, 1980 American Society for Metals and the Metallurgical Society of Aime, Volume 11A, June 1980.